



| | |
|-------------------------|--|
| Title | Locations and types of ruptures involved in the 2008 Sichuan earthquake inferred from SAR image matching |
| Author(s) | Kobayashi, Tomokazu; Takada, Youichiro; Furuya, Masato; Murakami, Makoto |
| Citation | Geophysical Research Letters, 36(7), L07302 https://doi.org/10.1029/2008GL036907 |
| Issue Date | 2009-04 |
| Doc URL | http://hdl.handle.net/2115/38133 |
| Rights | An edited version of this paper was published by AGU. Copyright 2009 American Geophysical Union. |
| Type | article (author version) |
| File Information | Kobayashi_GRL2009.pdf |



[Instructions for use](#)

**Locations and types of ruptures involved in
the 2008 Sichuan Earthquake
inferred from SAR image matching**

**Tomokazu Kobayashi,¹ Youichiro Takada,²
Masato Furuya,² and Makoto Murakami¹**

*¹Institute of Seismology and Volcanology, Graduate School of Science, Hokkaido
University, Kita 10 Nishi 8, Kita-ku, Sapporo 060-0810, Japan*

*²Department of Natural History Sciences, Graduate School of Science, Hokkaido
University, Kita 10 Nishi 8, Kita-ku, Sapporo 060-0810, Japan*

Tel +81-11-706-3552

Email tkoba@uvo.sci.hokudai.ac.jp

Submitted to *Geophysical Research Letters*

Abstract

1
2 We have detected detailed ground displacements in the proximity of the
3 Longmen Shan fault zone (LMSFZ) by applying a SAR offset-tracking method in the
4 analysis of the 2008 Sichuan earthquake. An elevation-dependent correction is
5 indispensable for achieving sub-meter accuracy. A sharp displacement discontinuity
6 with a relative motion of ~1-2 m appears over a length of 200 km along the LMSFZ,
7 which demonstrates that the main rupture has proceeded on the Beichuan fault (BF)
8 among several active faults composing the LMSFZ, and a new active fault is detected
9 on the northeastward extension of the BF. The rupture on the BF is characterized by a
10 right-lateral motion in the northeast, while in the southwest an oblique right-lateral
11 thrust slip is suggested. In contrast to the northeast, where a major rupture proceeded on
12 the BF only, in the southwest multiple thrust ruptures have occurred in the southeastern
13 foot of the Pengguan massif.

14

15

16 Keywords: 2008 Sichuan Earthquake, ground displacement, SAR offset-tracking

17 **1. Introduction**

18 A catastrophic earthquake with a moment magnitude of 7.9 struck China's
19 Sichuan area on 12 May 2008 [*U.S. Geological Survey, 2008*]. This earthquake could be
20 associated with the reactivation of the Longmen Shan fault zone (LMSFZ), running
21 over a length of 200 km along the western margin of the Sichuan Basin (Figure 1). The
22 fault zone consists of several faults dipping to the northwest that have been constructed
23 in the area subjected to contractional stress due to the eastward movement of the
24 Tibetan plateau [*Burchfiel et al., 2008*]. The faults have a complicated development in
25 and around the Pengguan massif (PM) (Figure 1). Three major active faults, indicated
26 by red lines in Figure 1 [*Densmore et al., 2007*], are running near the epicenter (red star)
27 located at the southwestern edge of the PM. The rupture is thought to proceed
28 northeastward along the fault zone as inferred from the extent of the aftershocks
29 reported by the U. S. Geological Survey (black dots in Figure 1), but it remains
30 uncertain where and how the faults were involved in the seismic event [*Burchfiel et al.,*
31 *2008*]. The measurement of ground displacements around the epicentral area certainly
32 plays a key role in answering these questions.

33 Satellite synthetic aperture radar (SAR) data can provide detailed and spatially
34 comprehensive ground information. Interferometric SAR (InSAR) analysis has an

35 advantage of detecting ground deformation in a vast region with high precision [e.g.,
36 *Massonnet and Feigl, 1998; Bürgmann et al., 2000*]. However, for the Sichuan event,
37 the standard InSAR approach is not helpful in knowing the faults directly related to the
38 seismic rupture. This is because the displacement amplitude near the fault zone was too
39 large and a coherent loss area which spreads over an area ~200 km long and ~10-30 km
40 wide prevents us from satisfactorily obtaining the ground deformation in the proximity
41 of the fault zone. Thus, in order to reveal the unknown surface displacements, we
42 conduct an offset-tracking procedure that enables us to robustly detect large ground
43 deformation even in an incoherent area [*Michel et al., 1999; Tobita et al., 2001; Pathier*
44 *et al., 2006*]. While similar approaches can be taken with optical images [e.g., *Avouac et*
45 *al., 2006*], SAR images are advantageous because of the radar's all-weather detection
46 capability.

47

48 **2. SAR Data Analysis**

49 We use ALOS/PALSAR data on the ascending orbital paths 471 to 476 (Table
50 S1) for data analysis. The data obtained is strip-map imagery with an incidence angle of
51 38.7°. The analyzed areas are indicated by blue frames in the inset of Figure 1. We
52 process the SAR data from a level-1.0 product using a software package Gamma

53 [Wegmüller and Werner, 1997]. After conducting coregistration between two images
54 acquired before and after the mainshock, we divide the single-look SAR amplitude
55 images into patches and calculate an offset between the corresponding patches by an
56 intensity tracking method. This method is performed by cross-correlating samples of
57 backscatter intensity of a master image with those of a slave image [Strozzi *et al.*, 2002].
58 We now employ a near-square search patch of 64×192 pixels (range \times azimuth, ~ 480
59 $m \times 610$ m on the ground) and a sampling interval of 36×108 pixels (~ 270 m \times 340 m
60 on the ground). The measured offset consists of two components: (1) displacement
61 along the line of sight (range offset) and (2) a horizontal movement on the ground,
62 parallel along the satellite track (azimuth offset).

63 Accuracy of offset measurement depends strongly on the quality of image
64 coregistration, and thus, we carry out an additional operation that is not necessary over a
65 flat area: a correction of stereoscopic effect [Michel *et al.*, 1999; Pathier *et al.*, 2006].
66 Besides the actual surface displacements, range offsets include artifact offsets over
67 rugged terrain, resulting from a difference in foreshortening effect caused by separation
68 between the satellite orbital tracks. Thus, we reduce the artifact by applying an
69 elevation-dependent correction incorporating SRTM (NASA's Shuttle Radar
70 Topography Mission) DEM data with a 3 arcsec resolution [Farr *et al.*, 2007].

71

72 **3. Ground displacements for the 2008 Sichuan Earthquake**

73 Figure 2 shows the estimated range offset field over the entire analyzed area.

74 The offset analysis succeeded in mapping the ground displacement in the proximity of

75 the fault zone, which was difficult to achieve from the standard InSAR approach. The

76 most notable feature is a sharp color discontinuity over a length of about 200 km, across

77 which the ground movement is in the opposite direction (solid line). The boundary

78 extends continuously in the northeast-southwest orientation, running just along the

79 LMSFZ. The movement in the northern side of the boundary is away from the satellite

80 (red), while that in the southern side is towards the satellite (blue). A major

81 displacement field is localized within a zone no wider than several tens of kilometers,

82 and the amount of relative displacement near the boundary reaches up to ~2 m. It should

83 now be noted that the displacement boundary is in very good agreement with the

84 Beichuan fault (BF) trace (dotted line), suggesting that a main rupture proceeded on the

85 BF. This is the first published information from satellite data that mentions the fault as a

86 major contributor to the earthquake rupture. Further a noteworthy accomplishment is

87 that we detected a new active fault. A displacement boundary clearly appears not only

88 on the BF trace (dotted line) which has been identified as an active fault [*Densmore et*

89 *al.*, 2007] but also on its northeastward extension (Figure 2). We stress that the location
90 of the active fault, namely the BF, is confirmed not from the geomorphological
91 observations but from the actual surface displacements associated with the earthquake.

92 The original azimuth offset field (Figure S1a) suffers from periodic offset
93 patterns that are presumably ionosphere-related noises [*Gray et al.*, 2000; *Wegmüller et*
94 *al.*, 2006]. In order to reduce the oscillatory noises, we apply a band-cut filter through
95 which the wavenumbers corresponding to the noises are removed. The detailed method
96 is shown in the auxiliary material (Figure S2). After filtering, in the azimuth offset field
97 (Figure S1b), displacement boundaries turn out to be in the proximity of the fault zone
98 (solid lines). However, the spatial pattern is slightly different from the range offset. In
99 the northeast of the fault zone, the displacement boundary overlaps the BF (dotted line)
100 and its extension in the same location as the range offset result, but in the southwest the
101 boundary on the BF is not clear and a new discontinuity is identified at a different
102 location. The rupture style of this seismic event seems to be more complex than that
103 expected from the range offset field. In the following, we focus on the paths 472 and
104 474, in which the azimuth noises are suppressed well by filtering, and investigate more
105 detailed features of the ruptures in the northeast and in the southwest.

106 The rupture type on the BF is different between in the northeast and in the

107 southwest. Figure 3a shows the offset field in the northeast of the BF (path 472) in
108 range (left) and azimuth (right). The range offset shows that the movement in the
109 northern side of the displacement boundary (solid line) is away from the satellite (red)
110 and that in the southern side is toward the satellite (blue), while for the azimuth offset
111 the movements in the northern and southern sides are toward (red) and opposite to
112 (blue) the satellite flight direction, respectively. Taking four simple fault types into
113 account; reverse, normal, right-lateral, and left-lateral motions, the fault motion that can
114 account for the observed displacement pattern is a right-lateral slip. The displacement
115 vector field, obtained from an assumption that the observed offsets are produced by only
116 horizontal movements on the ground, shows a nearly pure right-lateral fault motion of
117 approximately 2 m (Figure S3).

118 On the other hand, in the southwest on the BF (path 474) the fault motion is
119 slightly more complex (Figure 3b). A displacement boundary on the BF that is observed
120 from both the offset fields in the northeast (Figure 3a) is not distinct in the azimuth field
121 (Figure 3b, right), although the boundary is clearly visible in the range (solid line in
122 Figure 3b, left). This suggests that the observed displacement can be explained by
123 neither a pure dextral strike-slip nor a pure reverse fault motion. The preferred rupture
124 style is a composite motion including both right-lateral and reverse slip components.

125 The outline of the inferred fault motions is illustrated in Figure 4. The obtained
126 offset field reveals that the main rupture occurred on the BF and its rupture style is
127 characterized by a right-lateral motion in the northeast and an oblique right-lateral thrust
128 slip in the southwest. The result inferred from the offset analysis has a good agreement
129 with that of the preliminary teleseismic waveform analysis showing that the Sichuan
130 event slipped right-laterally in the northeast and in the southwest with a right-lateral
131 thrust component [e.g., *Nishimura and Yagi, 2008*]. The difference in the northeast and
132 southwest fault-motion types may suggest that the BF is segmented at the north end of
133 the PM, which corresponds to a geological boundary [*Burchfiel et al., 2008*].

134 In contrast to the northeastern part of the LMSFZ where the observations can
135 be accounted for a relatively simple motion on the BF, the offset fields in the southwest
136 are suggestive of complicated ground deformations. In the southeastern flank of the PM
137 (inset of Figure 3b), a clear displacement boundary with a relative motion of nearly 1 m
138 can be observed over a length of ~50 km in the azimuth offset field (arrows in right
139 panel). A large offset of ~2 m moving toward the satellite, featured with arrows (inset in
140 left panel of Figure 3b), appears around the corresponding area in the range offset field.
141 The deforming area is obviously distant from the BF (dotted line in the inset), thus
142 indicating occurrence of another regional rupture. The detected rupture is traced near

143 the Pengguan fault (PF) as mapped by *Densmore et al.* [2007] but does not completely
144 correspond to the PF trace in the azimuth offset (dotted line in Figure 3b). Thus we do
145 not argue at present to what extent the deformation is related to the PF.

146 The displacement pattern of the regional deformation is evidently different
147 from that observed along the BF. In the azimuth field, the movement in the northern
148 side of the boundary is opposite to the satellite flight direction (blue), while that in the
149 southern side is toward the flight direction (red). Thus a convergent motion is suggested
150 because a left-lateral motion is unlikely. There is no clear displacement discontinuity in
151 the range, indicating no significant strike-slip motion but probably an upheaval. Thus
152 we can say that the local deformation is of a reverse fault type. The offset result shows
153 that in the southwest of the LMSFZ, multiple ruptures which are different fault motions
154 but significantly include reverse slip components occurred (Figure 4).

155 On the other hand, there is no signal showing any significant ground
156 deformations along the Wenchuan-Maowen fault (WMF), which is one of the major
157 active faults composing the LMSFZ. The idea that no significant rupture occurred on
158 the WMF is in harmony with the observation that the aftershocks mainly distribute
159 around the BF rather than the WMF (Figure 1).

160 With the knowledge of the locations of main ruptures, we constructed a

161 preliminary fault model that consists of three rectangular faults with distributed slips,
162 using an elastic half-space dislocation model [Okada, 1992] (Table S2). The synthetic
163 range offset field obtained from our preliminary fault model reproduces roughly the
164 observed spatial pattern on the offset field (Figure S4). In our model, a right-lateral
165 motion is dominant in the northeast of the BF (Figure S5a; F1), while in the southwest
166 an oblique slip consisting of right-lateral and reverse motions is assumed (Figure S5b;
167 F2). The rupture locally occurring near the PF is explained by a nearly pure thrust
168 motion (Figure S5c; F3). However, there still remain significant discrepancies between
169 the observed and calculated offset fields. A joint analysis with InSAR-based far-field
170 displacements data will allow us to infer more quantitative and detailed fault model, and
171 is deferred for future studies.

172

173 **4. Uncertainties and reliabilities of measured offsets**

174 To confirm how much errors are included in the measured offset fields, we
175 calculate offsets using two preseismic images for the paths 472 and 474, which have
176 almost the same perpendicular baseline (B_{perp}) as the coseismic image pairs shown in
177 Figure 3 (Table S1). Preseismic offset fields have little displacement (Figure S6),
178 suggesting that the observed coseismic offsets exceed the potential error level

179 significantly. The offset values in the basin are nearly zero; the root mean square (RMS)
180 values are estimated to be ~ 0.1 m for both paths, but those in the mountains are not
181 necessarily zero, particularly in high elevation areas; the RMS values are ~ 0.3 and ~ 0.4
182 m, for the paths 472 and 474, respectively. This may be because a correction of
183 stereoscopic effect is insufficient because of the large amount of topographic relief. It is
184 further noted that the displacement boundaries shown in Figure 3 are not seen in the
185 preseismic data. This justifies our claim that the observed boundaries are not artifact but
186 actual surface changes associated with the seismic event.

187 The SAR images that include mountainous areas suffer strongly from
188 foreshortening effects because of steep topography, which produces severe image
189 distortion. Figure S7 shows the offset fields for the paths (a) 472 and (b) 474 calculated
190 using the same preseismic data of Figure S6 but with no elevation-dependent correction.
191 Considerable offset errors, locally in excess of 3 m, correlating with the elevation are
192 included. Although in principle the offset error caused by a stereoscopic effect should
193 affect high topographic areas only, the poor global image coregistration resultantly gives
194 more errors to the basin area as well. This result demonstrates that an
195 elevation-dependent correction is indispensable for mountainous environments for
196 extracting surface changes with high precision.

197

198 **5. Summary**

199 We have successfully obtained ground displacements in the proximity of the
200 Longmen Shan fault zone (LMSFZ) by an offset-tracking method, after applying an
201 elevation-dependent correction. The outline of the inferred fault motions is illustrated in
202 Figure 4 and the analysis results are summarized below.

203 (1) A sharp displacement boundary, across which the ground movement is in
204 the opposite direction, appears northeastward over a length of 200 km along the
205 LMSFZ.

206 (2) The main rupture has proceeded on the Beichuan fault (BF) among the
207 several active faults composing the LMSFZ.

208 (3) A new active fault is detected on the northeastward extension of the BF.

209 (4) The rupture type is characterized by a right-lateral motion in the northeast
210 on the BF, while an oblique slip consisting of right-lateral and reverse motions is
211 suggested in the southwest.

212 (5) Multiple ruptures including significant reverse slips occurred in the
213 southeastern foot of the Pengguan massif.

214

215

216 **Acknowledgments**

217 PALSAR level 1.0 data were provided from the Earthquake Working Group
218 and PIXEL (PALSAR Interferometry Consortium to Study our Evolving Land surface)
219 under a cooperative research contract with JAXA (Japan Aerospace Exploration
220 Agency). The ownership of PALSAR data belongs to METI (Ministry of Economy,
221 Trade and Industry) and JAXA. This study is supported from KAKENHI (19340123
222 and 20900002). We thank two anonymous reviewers and the editor (Dr. Florindo) for
223 their helpful comments to improve our manuscript.

224

225

226 **References**

- 227 Avouac, J. P., F. Ayoub, S. Leprince, O. Konca, and D. V. Helmberger (2006), The 2005,
228 Mw 7.6 Kashmir earthquake: Sub-pixel correlation of ASTER images and seismic
229 waveforms analysis, *Earth Planet Sci. Lett.*, *249*, 516-528.
- 230 Burchfiel, B. C., L. H. Royden, R. D. van der Hilst, B. H. Hager, Z. Chen, R. W. King,
231 C. Li, J. Lü, H. Yao, and E. Kirby (2008), A geological and geophysical context for
232 the Wenchuan earthquake of 12 May 2008, Sichuan, People's Republic of China,
233 *GSA Today*, *18*, 4 –11, doi:10.1130/GSATG18A.1.
- 234 Bürgmann, R., P. A. Rosen, and E. J. Fielding (2000), Synthetic Aperture radar
235 interferometry to measure Earth's surface topography and its deformation, *Annu.*
236 *Rev. Earth Planet. Sci.*, *28*, 169– 209.
- 237 Densmore, A. L., M. A. Ellis, Y. Li, R. Zhou, G. S. Hancock, and N. Richardson (2007),
238 Active tectonics of the Beichuan and Pengguan faults at the eastern margin of the
239 Tibetan Plateau, *Tectonics*, *26*, doi: 10.1029/2006TC001987.
- 240 Farr, T. G., P. A. Rosen, E. Caro, R. Crippen, R. Duren, S. Hensley, M. Kobrick, M.
241 Paller, E. Rodriguez, L. Roth, D. Seal, S. Shaffer, J. Shimada, J. Umland, M. Werner,
242 M. Oskin, D. Burbank, and D. Alsdorf (2007), The Shuttle Radar Topography
243 Mission, *Rev. Geophys.*, *45*, doi: 1029/2005RG000183.

- 244 Gray, A. L., D. E. Mattar, and G. Sofko (2000), Influence of ionospheric electron
245 density fluctuations on satellite radar interferometry, *Geophys. Res. Lett.*, 27,
246 1415-1454.
- 247 Massonnet, D. and K. L. Feigl (1998), Radar interferometry and its application to
248 changes in the earth's surface, *Rev. Geophys.*, 36, 441– 500.
- 249 Michel, R., J. P. Avouac, and J. Taboury (1999), Measuring ground displacements from
250 SAR amplitude images: application to the Landers earthquake, *Geophys. Res. Lett.*,
251 26, 875-878.
- 252 Nishimura, N. and Y. Yagi (2008), Rupture process for May 12, 2008 Sichuan
253 earthquake (preliminary result),
254 <http://www.geol.tsukuba.ac.jp/~nisimura/20080512/>.
- 255 Okada, Y. (1992), Internal deformation due to shear and tensile faults in a half-space,
256 *Bull. Seismol. Soc. Am.*, 82, 1018-1040.
- 257 Pathier, E., E. J. Fielding, T. J. Wright, R. Walker, B. E. Parsons, and S. Hensley (2006),
258 Displacement field and slip distribution of the 2005 Kashmir earthquake from SAR
259 imagery, *Geophys. Res. Lett.*, 33, doi: 10.1029/2006GL027193.
- 260 Strozzi, T., A. Luckman, T. Murray, U. Wegmuller, and C. L. Werner (2002), Glacier
261 motion estimation using SAR offset-tracking procedures, *IEEE Trans. Geosci.*
262 *Remote Sens.*, 40, 2384-2391.

- 263 Tobita, M., M. Murakami, H. Nakagawa, H. Yarai, S. Fujiwara, and P. A. Rosen (2001),
264 3-D surface deformation of the 2000 Usu eruption measured by matching of SAR
265 images, *Geophys. Res. Lett.*, 28, 4291-4294.
- 266 U.S. Geological Survey Earthquake Center (2008), National Earthquake Information
267 Center: <http://earthquake.usgs.gov/eqcenter/eqinthenews/2008/us2008ryan>.
- 268 Wegmüller, U. and C. L. Werner (1997), Gamma SAR processor and interferometry
269 software, in Proceedings of the 3rd ERS Symposium, Eur. Space Agency Spec.
270 Publ., ESA SP-414, 1686–1692.
- 271 Wegmüller, U., C. Werner, T. Strozzi, and A. Wiesmann (2006), Ionospheric electron
272 concentration effects on SAR and INSAR, Proceeding of IGARSS 2006, Denver, 31
273 July-4 August.

274 **Figure captions**

275 Figure 1 Tectonic setting of the Longmen Shan fault zone. Topographic relief map is
276 taken from the SRTM DEM data with a resolution of 3 arcsecs. Light green colored
277 areas in the relief indicate lacks of DEM data. The epicenter is marked with a star,
278 and the aftershocks that occurred from 12-19 May are shown as black dots [*U.S.*
279 *Geological Survey, 2008*]. Solid lines are fault traces drawn after *Densmore et al.*
280 [2007], and the red lines stand for the Wenchuan-Maowen, Beichuan, and Pengguan
281 faults, which are active faults that compose the majority of the Longmen Shan fault
282 zone. Analyzed regions are indicated by blue frames in the inset.

283

284 Figure 2 Displacement field in range component. Warm and cold colors represent
285 displacements away from and toward the satellite, respectively. A sharp color
286 discontinuity, across which the ground motion is in the opposite direction, is
287 highlighted with a solid line, and is recognized to be just along the Beichuan fault
288 trace indicated by a dotted line.

289

290 Figure 3 Displacement field for the paths (a) 472 and (b) 474 in (left) range and (right)
291 azimuth components, respectively. In the range offset field, warm and cold colors

292 stand for displacements away from and toward the satellite, respectively, and in the
293 azimuth toward and opposite the satellite flight direction, respectively. Displacement
294 boundaries are highlighted with solid lines. Arrows in the inset of the range and
295 azimuth fields features a deforming area located at the southeastern foot of the
296 Pengguan massif. WMF: Wenchuan-Maowen fault, BF: Beichuan fault, PF:
297 Pengguan fault, and PM: Pengguan massif.

298

299 Figure 4 Schematic fault motions inferred from the offset fields. BF: Beichuan fault and
300 PM: Pengguan massif.

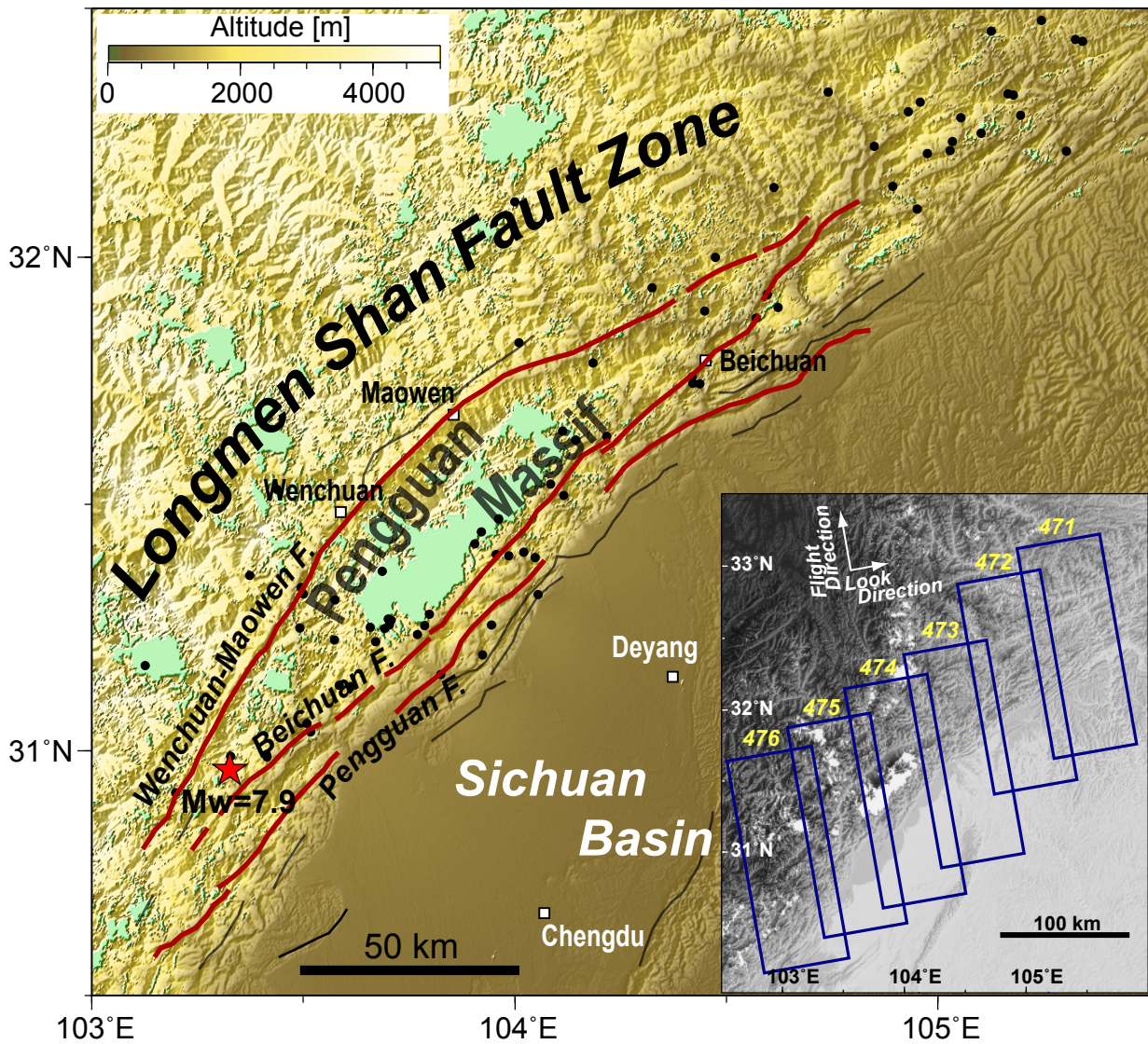


Figure 1 Tectonic setting of the Longmen Shan fault zone. Topographic relief map is taken from the SRTM DEM data with a resolution of 3 arcsecs. Light green colored areas in the relief indicate lacks of DEM data. The epicenter is marked with a star, and the aftershocks that occurred from 12-19 May are shown as black dots [U.S. Geological Survey, 2008]. Solid lines are fault traces drawn after Densmore et al. [2007], and the red lines stand for the Wenchuan-Maowen, Beichuan, and Pengguan faults, which are active faults that compose the majority of the Longmen Shan fault zone. Analyzed regions are indicated by blue frames in the inset.

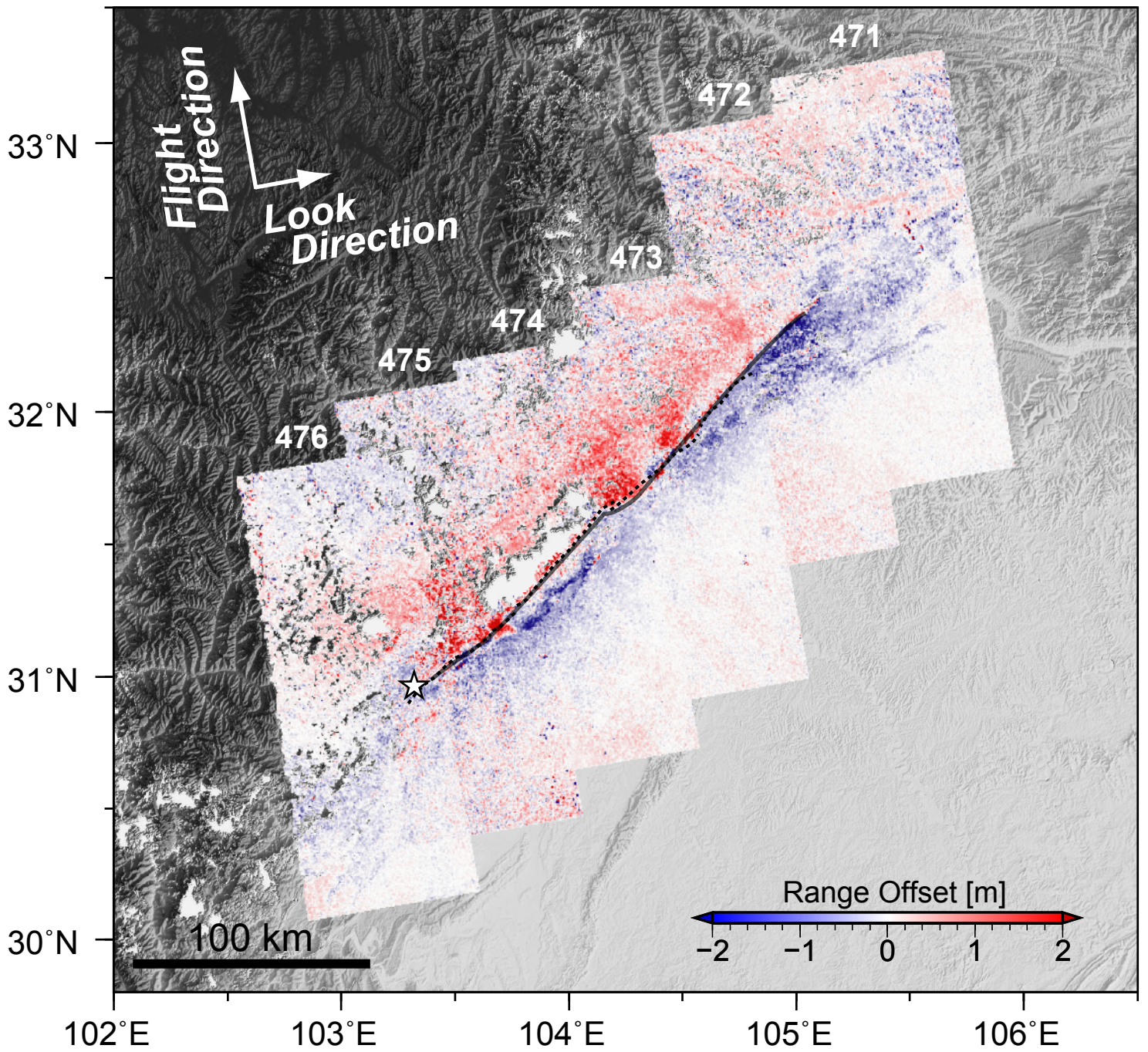


Figure 2 Displacement field in range component. Warm and cold colors represent displacements away from and toward the satellite, respectively. A sharp color discontinuity, across which the ground motion is in the opposite direction, is highlighted with a solid line, and is recognized to be just along the Beichuan fault trace indicated by a dotted line.

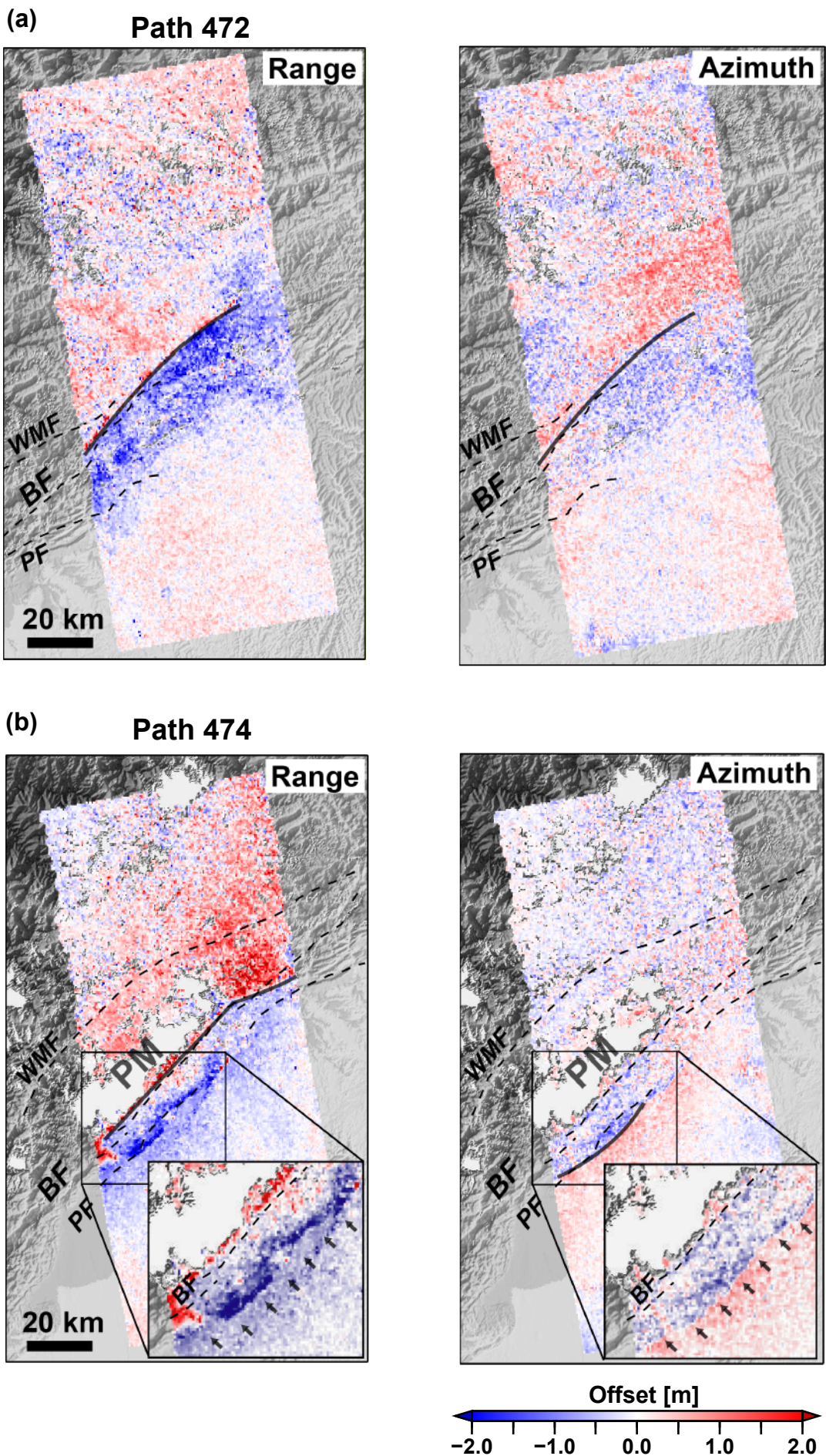


Figure 3 Displacement field for the paths (a) 472 and (b) 474 in (left) range and (right) azimuth components, respectively. In the range offset field, warm and cold colors stand for displacements away from and toward the satellite, respectively, and in the azimuth toward and opposite the satellite flight direction, respectively. Displacement boundaries are highlighted with solid lines. Arrows in the inset of the range and azimuth fields features a deforming area located at the southeastern foot of the Pengguan massif. WMF: Wenchuan-Maowen fault, BF: Beichuan fault, PF: Pengguan fault, and PM: Pengguan massif.

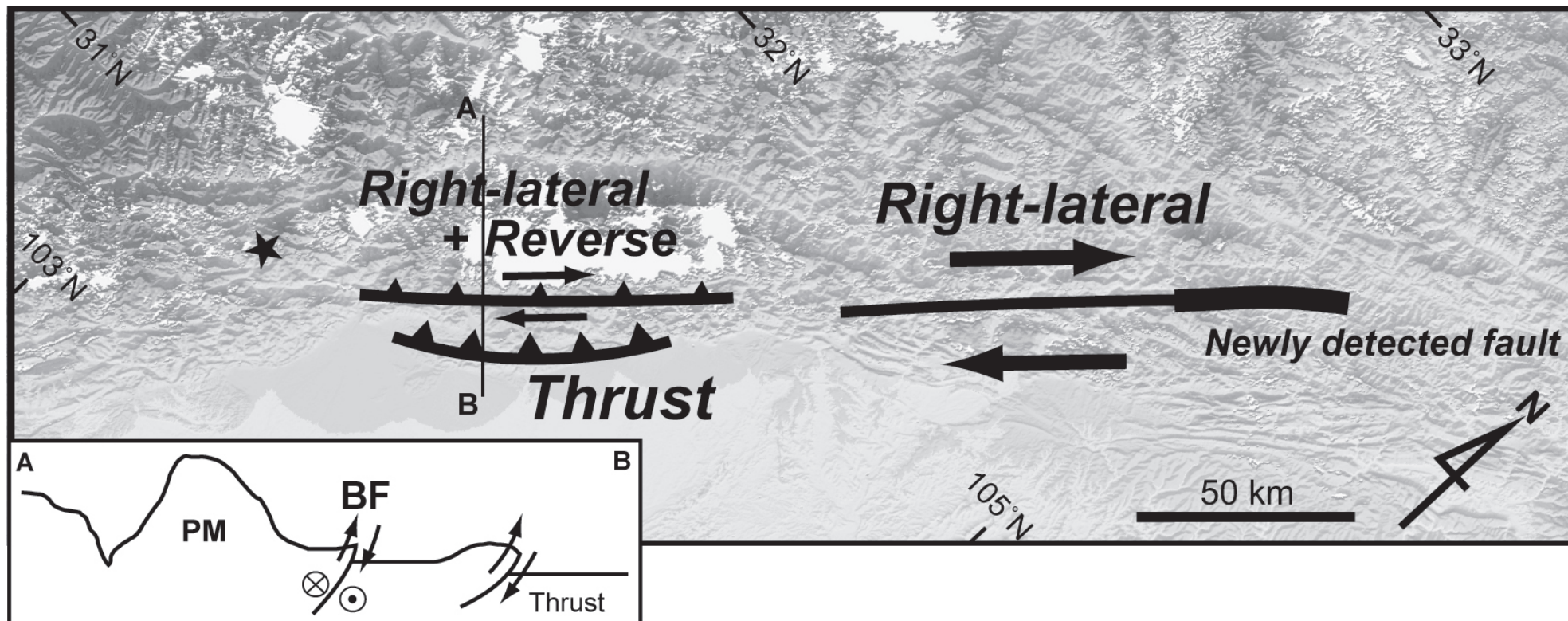


Figure 4 Schematic fault motions inferred from the offset fields. BF: Beichuan fault and PM: Pengguan massif.

1 Auxiliary Material Submission for Paper 2008GLXXXXXX

2 Locations and types of ruptures involved in the 2008 Sichuan Earthquake inferred
3 from SAR image matching.

4 Tomokazu Kobayashi,^{*} Youichiro Takada,^{**} Masato Furuya,^{**} and Makoto Murakami^{*}

5 (^{*}Institute of Seismology and Volcanology, Graduate School of Science, Hokkaido

6 University, Sapporo 060-0810, Japan

7 ^{**}Department of Natural History Sciences, Graduate School of Science, Hokkaido

8 University, Sapporo 060-0810, Japan)

9 Geophys. Res. Lett., X (X), doi: 10.1029/2008GLXXXXXX, 200X

10
11 Introduction

12 This auxiliary material contains (1) the azimuth offset fields covering the overall
13 seismic areas, (2) a filtering method for reducing the azimuth streaks, (3) a horizontal
14 displacement vector for the path 472, (4) a comparison between the observed and
15 synthetic range offset fields, (5) slip distributions obtained from our preliminary fault
16 model, (6) offset fields for preseismic data pairs for the paths 472 and 474, (7)
17 preseismic offset fields without elevation-dependent correction for the paths 472 and
18 474, (8) the information list of acquired SAR data, and (9) list of parameters for the
19 preliminary fault model. The offsets given in auxiliary materials are measured in the
20 same manner as those shown in Figures 2 and 3.

21 Figure S1 is given in the JPEG file entitled “2008glXXXXXX-fs01.jpg”. The azimuth
22 offset field suffers from periodic stripes with an amount of 4-5 m, which are presumably
23 the ionosphere-related noise (Figure S1a) [*Gray et al.*, 2000; *Wegmüller et al.*, 2006]. In
24 order to reduce the oscillatory noise, we applied a band-cut filter through which the

25 wavenumber corresponding to the noise is eliminated (Figure S1b). The filtering
26 procedure we conducted is explained in Figure S2. Although the streaks are not
27 completely removed in some images, displacement boundaries appear in the proximity
28 of the fault zone (solid lines). This filtering approach does not solve the problem on the
29 azimuth streaks substantially, but it is very useful to obtain the spatial pattern of surface
30 changes practically.

31 Figure S2 is given in the JPEG file entitled “2008glXXXXXX-fs02.jpg”. We now
32 explain the filtering procedure through which the azimuth streaks are reduced. The
33 azimuth offset data of the path 472 is shown as an example in Figure S2. Figures S2a
34 and S2d show the original observed azimuth offset field and its power spectrum in
35 spatial frequency domain obtained by applying a 2D Fourier transform (FT),
36 respectively. Strong powers are recognized at the four corners corresponding to a
37 low-frequency domain, and among them the powers at the two corners, indicated by
38 circles, correspond to the azimuth streaks. We cut the powers off and apply a 2D inverse
39 Fourier transform (IFT) to the remaining frequency components (Figure S2e), and then
40 we can obtain the azimuth offset field in which the oscillatory noise is suppressed
41 (Figure S2b). A high-cut filter is further applied to avoid the aliasing effect and to obtain
42 a spatially smoothed offset field by cutting high frequency noises, as the need arises.
43 Figure S2c shows the modeled azimuth streaks that are constructed from the removed
44 frequency components (Figure S2f). We emphasize that such a simple operation can
45 conveniently provide us the actual ground displacement concealed under the azimuth
46 streaks.

47 Figure S3 is given in the JPEG file entitled “2008glXXXXXX-fs03.jpg”. Taking into
48 account that the fault motion for the path 472 is of strike-slip, displacement vectors are

49 drawn under an assumption that the observed offsets are produced only by horizontal
50 movements on the ground. In order to stabilize the vector field, we average the offsets
51 within a window of 30×30 pixels, which is set with a sampling interval of 30 pixels in
52 the range and azimuth fields, respectively, and then vectorize them. The vector field is
53 of a right-lateral fault motion, but it shows displacements that are strongly asymmetrical
54 with much larger displacements on the southeast side of the fault than on the northwest
55 side. Yellow arrows indicate the displacement vectors calculated using the data of the
56 neighboring path (473). The displacement vector field including the data of path 473
57 shows a nearly symmetrical right-lateral motion. The displacements in the southeast
58 side of the fault are consistent between the paths 472 and 473, but in the northwest side
59 there is a large difference between the two. The data of path 473 was acquired one week
60 after the earthquake occurrence, while that of path 472 was acquired one month after the
61 earthquake (Table S1). This discrepancy in the displacement may suggest that other
62 regional motions occurred in this mountainous area after the earthquake, which may not
63 occur on the BF. The assumption of pure horizontal motion may not necessarily be
64 applied to the data of path 472 in this area.

65 Figure S4 is given in the JPEG file entitled “2008glXXXXXX-fs04.jpg”. We
66 construct a preliminary fault model that consists of three rectangular faults with
67 distributed slips, using an elastic half-space dislocation model [Okada, 1992]. We
68 separated the BF into two parts (F1 and F2) and additionally put a fault near the PF (F3).
69 We now use the range offsets only for modeling. The fault parameters are not derived
70 by any inversion techniques, but are manually assigned so that the calculated offset
71 fields are largely consistent with the observations.

72 Figure S5 is given in the JPEG file entitled “2008glXXXXXX-fs05.jpg”.

73 Figure S6 is given in the JPEG file entitled “2008glXXXXXXXX-fs06.jpg”. The offset
74 fields are calculated using the preseismic data pairs. The SAR scenes in Figure S6a
75 were acquired on 16 December 2007 and 31 January 2008, and in Figure S6b on 19
76 January 2008 and 5 March 2008, respectively. The perpendicular baselines are almost
77 the same as those for coseismic data pairs (Figure 3), which means that the stereoscopic
78 effects are comparable with one another.

79 Figure S7 is given in the JPEG file entitled “2008glXXXXXXXX-fs07.jpg”. The offset
80 fields for the paths 472 and 474 are calculated using the same preseismic data used for
81 Figure S6 but with no elevation-dependent correction.

82 Table S1 is given in the text file entitled “2008glXXXXXXXX-ts01.txt”. The acquisition
83 date, the observation modes handled by ALOS/PALSAR, and the perpendicular baseline
84 are listed in Table S1. FBS and FBD indicate the fine-beam single polarization and the
85 fine-beam dual polarization, respectively. Bperp stands for perpendicular baseline.

86 Table S2 is given in the text file entitled “2008glXXXXXXXX-ts02.txt”. Fault
87 parameters of the preliminary model (Figures S4 and S5) are listed. The location of each
88 fault is defined as its center. The strike is measured clockwise from the north.

89

90

91 1. 2008glXXXXXXXX-fs01.jpg (Figure S1) Azimuth offset fields for (a) original and (b)
92 band-cut filtered images. Solid and dotted lines in Figure S1b indicate displacement
93 boundaries across which the ground motion is in the opposite direction and a trace of
94 the Beichuan fault [Densmore *et al.*, 2007], respectively.

95

96 2. 2008glXXXXXXXX-fs02.jpg (Figure S2) A filtering procedure for azimuth streaks. (a)

97 an original observed azimuth offset field, (b) a filtered azimuth offset field, (c) modeled
98 azimuth streaks, and (d-f) power spectra corresponding to (a-c), respectively. Frequency
99 components surrounded by circles correspond to the azimuth streaks.

100

101 3. 2008glXXXXXXXX-fs03.jpg (Figure S3) Horizontal displacement vectors for the area
102 corresponding to the path 472. The vectors are calculated under an assumption that the
103 observed offsets are produced only by horizontal movement on the ground. Red and
104 yellow arrows represent the displacement vectors calculated using the data of paths 472
105 and 473, respectively. A solid line indicates the displacement boundary observed in
106 offset fields.

107

108 4. 2008glXXXXXXXX-fs04.jpg (Figure S4) (a) Observed and (b) synthetic range offset
109 fields. Frames indicate the fault positions projected onto the surface. Thick lines
110 represent upper edge of each fault.

111

112 5. 2008glXXXXXXXX-fs05.jpg (Figure S5) Slip distributions for (a) F1, (b) F2, and (c) F3
113 shown in Figure S4, respectively. Arrows stand for the inferred slip vectors.

114

115 6. 2008glXXXXXXXX-fs06.jpg (Figure S6) Preseismic offset fields calculated by
116 conducting an elevation-dependent correction. The SAR scenes were acquired on 16
117 December 2007 and 31 January 2008 for the path 472 (a) and on 19 January 2008 and 5
118 March 2008 for the path 474 (b).

119

120 7. 2008glXXXXXXXX-fs07.jpg (Figure S7) Same as Figure S6 but with no

121 elevation-dependent correction.

122

123 8. 2008glXXXXXXXX-ts01.txt (Table S1) ALOS/PALSAR images.

124 8.1 Column "Path", orbital track number.

125 8.2 Column "Date_Master", acquisition date of master image.

126 8.3 Column "Mode_Master", observation mode for master image.

127 8.4 Column "Date_Slave", acquisition date of slave image.

128 8.5 Column "Mode_Slave", observation mode for slave image.

129 8.6 Column "Bperp", m, perpendicular baseline.

130

131 9. 2008glXXXXXXXX-ts02.txt (Table S2) Fault parameters of our preliminary model

132 shown in Figures S4 and S5.

133 9.1 Column "FLT", fault name.

134 9.2 Column "Lon", degrees, longitude of fault center.

135 9.3 Column "Lat", degrees, latitude of fault center.

136 9.4 Column "Depth", km, depth of fault center.

137 9.5 Column "Length", km, length of fault.

138 9.6 Column "Width", km, width of fault.

139 9.7 Column "Strike", degrees, strike direction of fault.

140 9.8 Column "Dip", degrees, dip angle of fault.

141

142

143 References:

144 Densmore, A. L., M. A. Ellis, Y. Li, R. Zhou, G. S. Hancock, and N. Richardson (2007),

145 Active tectonics of the Beichuan and Pengguan faults at the eastern margin of the
146 Tibetan Plateau, *Tectonics*, 26, doi:10.1029/2006TC001987.

147 Gray, A.L., D.E. Mattar, and G. Sofko (2000), Influence of ionospheric electron density
148 fluctuations on satellite radar interferometry, *Geophys. Res. Lett.*, 27, 1451-1454.

149 Okada, Y. (1992), Internal deformation due to shear and tensile faults in a half-space,
150 *Bull. Seismol. Soc. Am.*, 82, 1018-1040.

151 Wegmüller, U., C. Wener, T. Strozzi, and A. Wiesmann (2006), Ionospheric electron
152 concentration effects on SAR and INSAR, Proceeding of IGARSS 2006, Denver, 31
153 July-4 August.

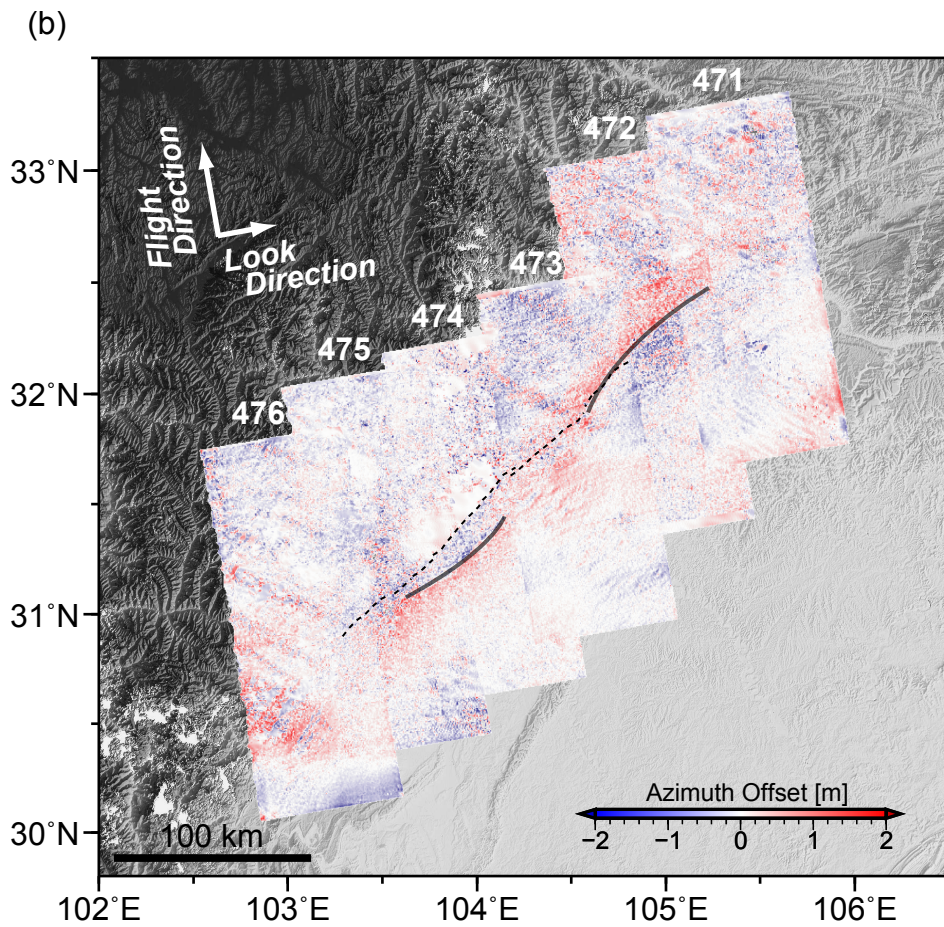
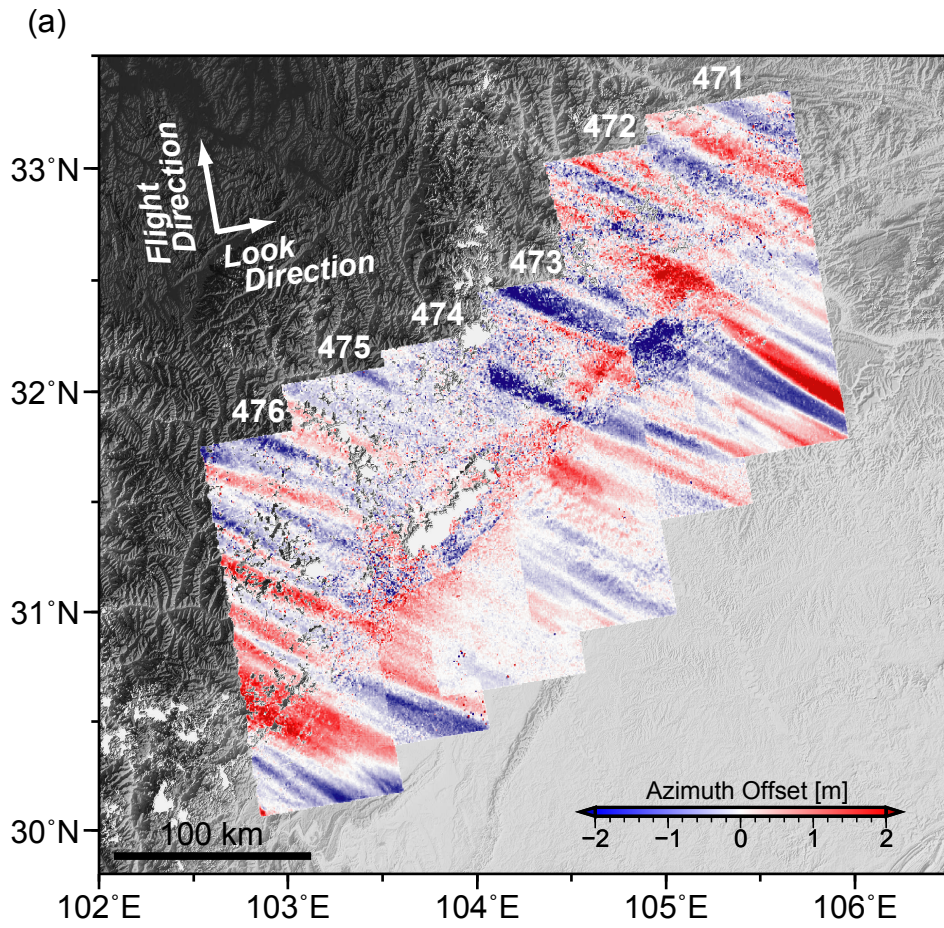


Figure S1 Azimuth offset fields for (a) original and (b) band-cut filtered images. Solid and dotted lines in Figure S1b indicate displacement boundaries across which the ground motion is in the opposite direction and a trace of the Beichuan fault [Densmore et al., 2007], respectively.

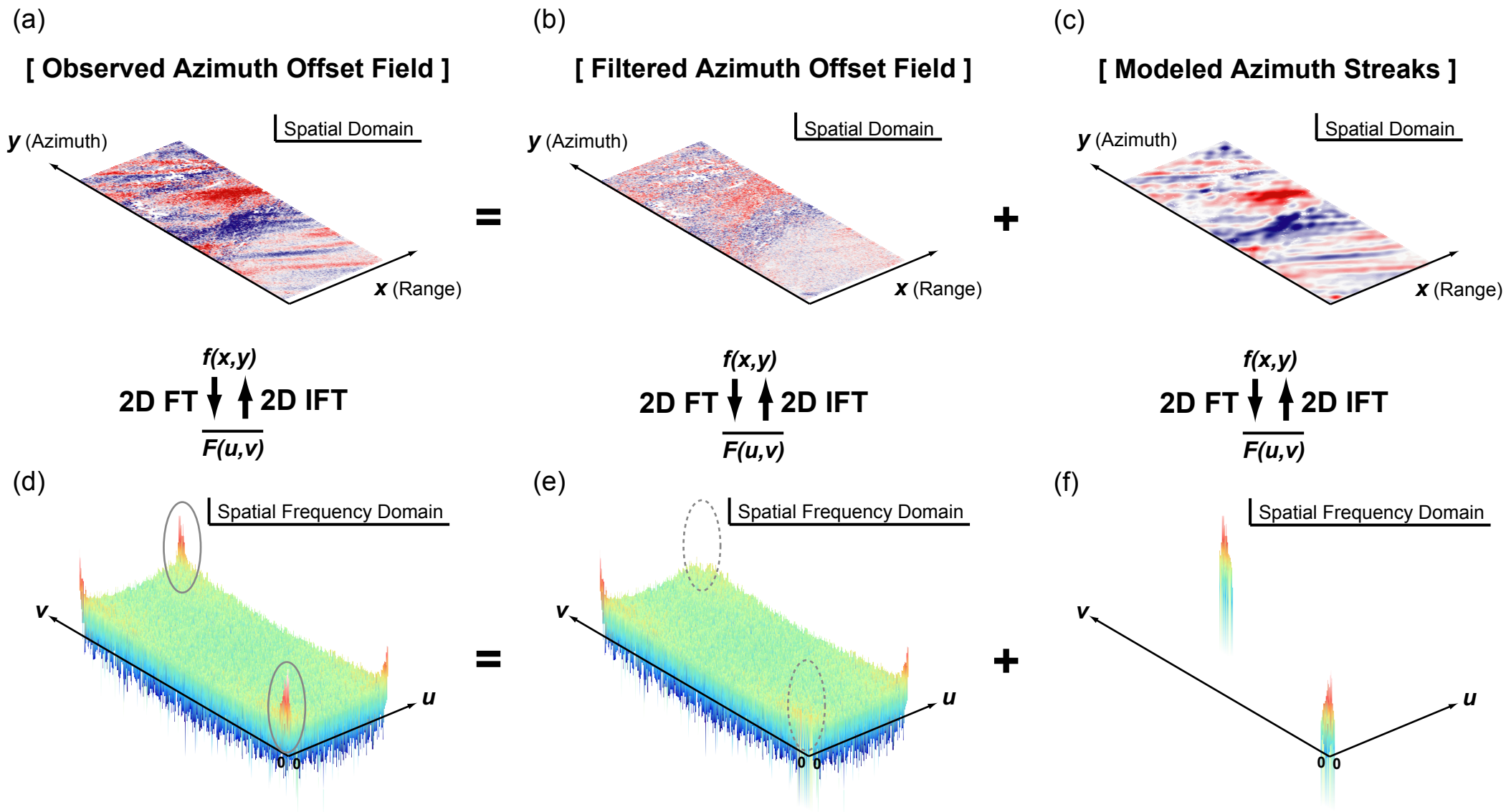


Figure S2 A filtering procedure for azimuth streaks. (a) an original observed azimuth offset field, (b) a filtered azimuth offset field, (c) modeled azimuth streaks, and (d-f) power spectra corresponding to (a-c), respectively. Frequency components surrounded by circles correspond to the azimuth streaks.

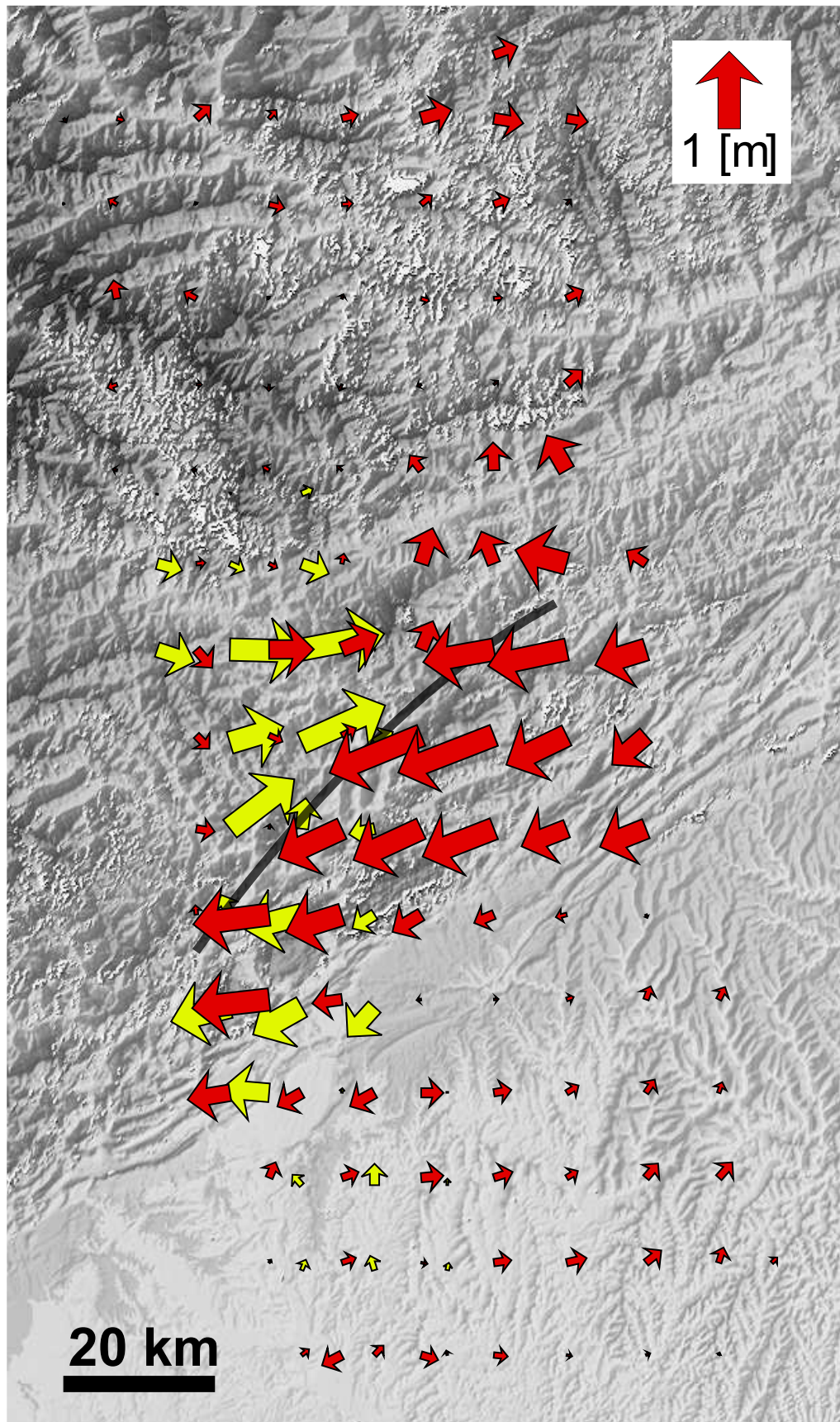


Figure S3 Horizontal displacement vectors for the area corresponding to the path 472. The vectors are calculated under an assumption that the observed offsets are produced only by horizontal movement on the ground. Red and yellow arrows represent the displacement vectors calculated using the data of paths 472 and 473, respectively. A solid line indicates the displacement boundary observed in offset fields.

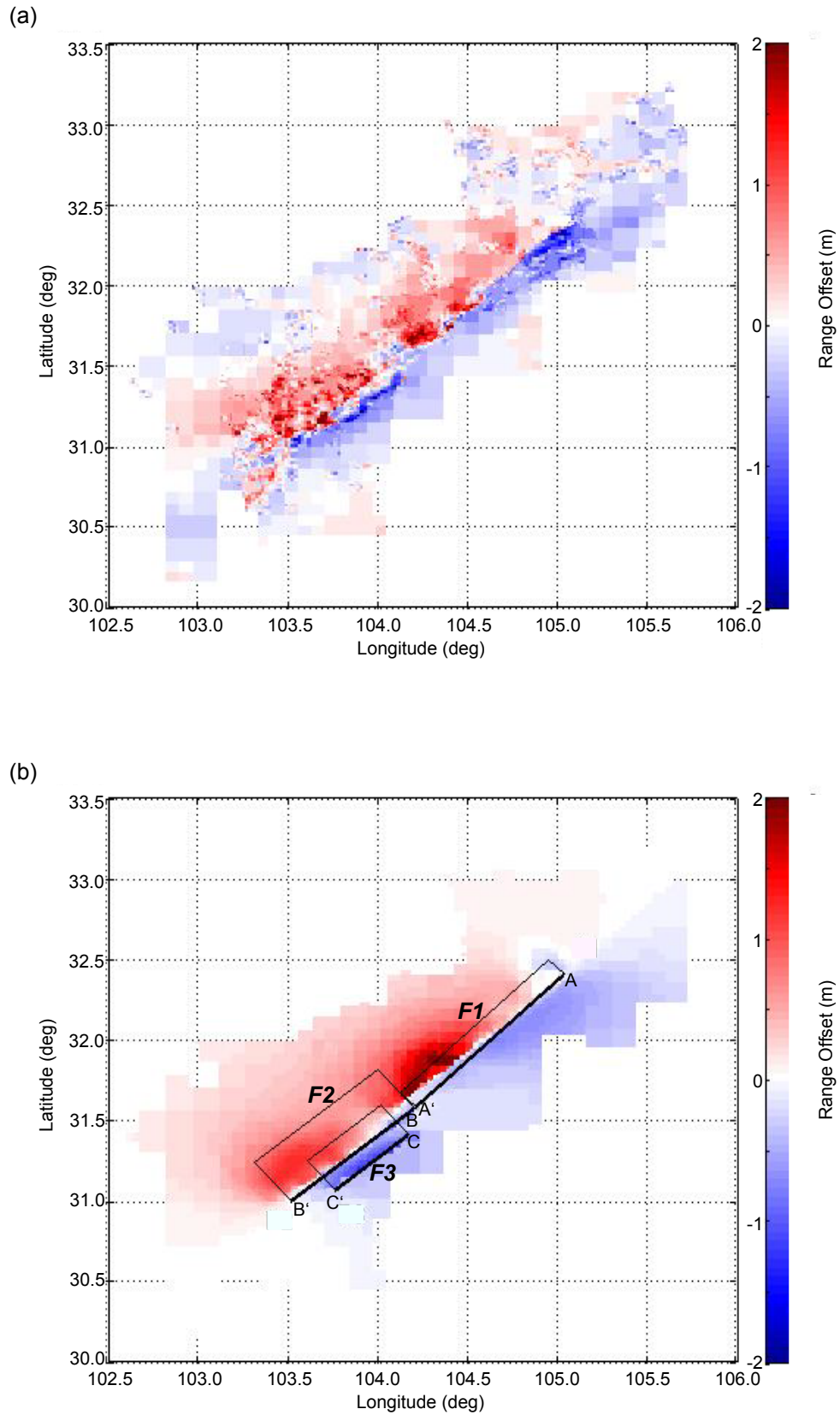


Figure S4 (a) Observed and (b) synthetic range offset fields. Frames indicate the fault positions projected onto the surface. Thick lines represent upper edge of each fault.

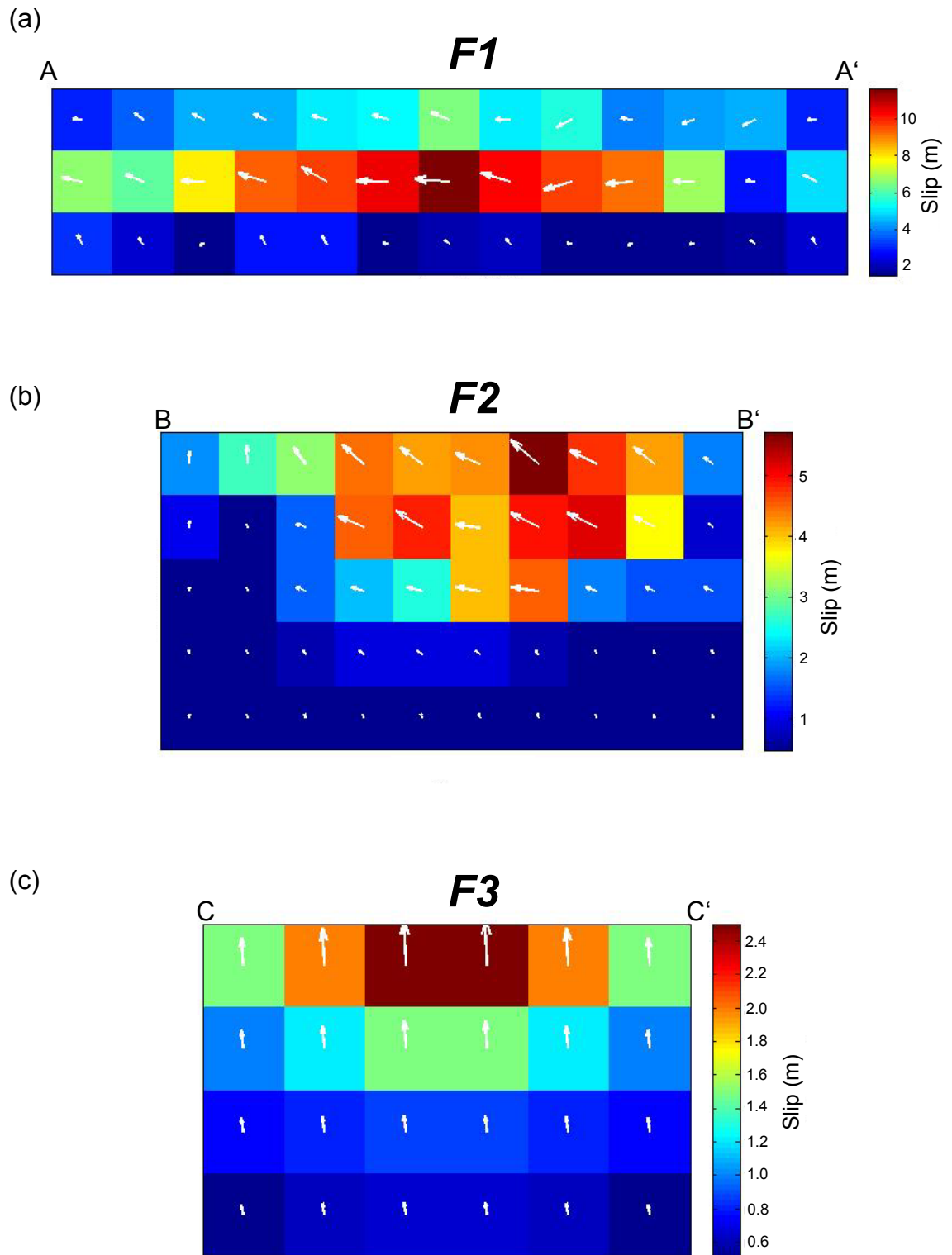


Figure S5 Slip distributions for (a) F1, (b) F2, and (c) F3 shown in Figure S4, respectively. Arrows stand for the inferred slip vectors.

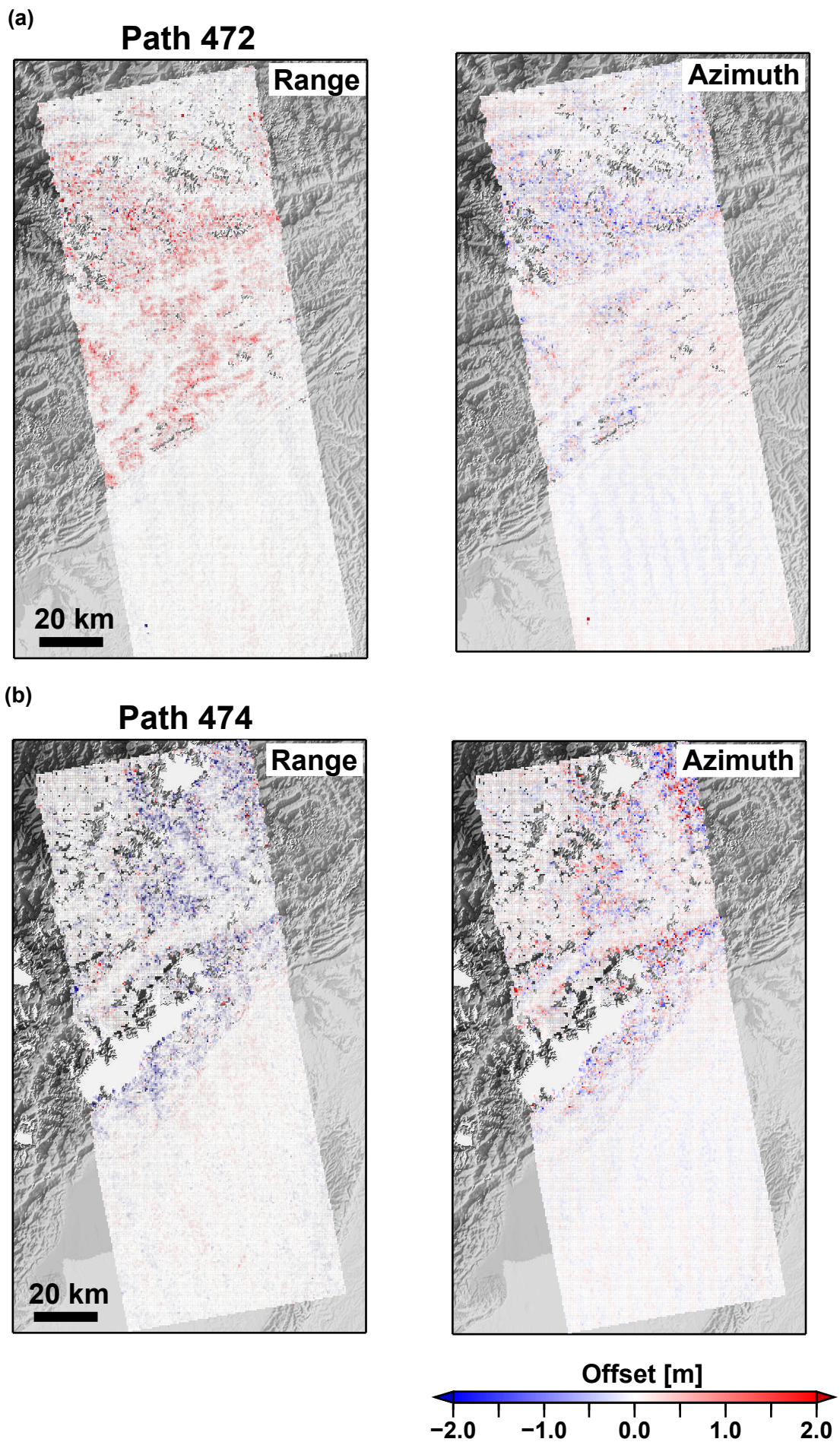
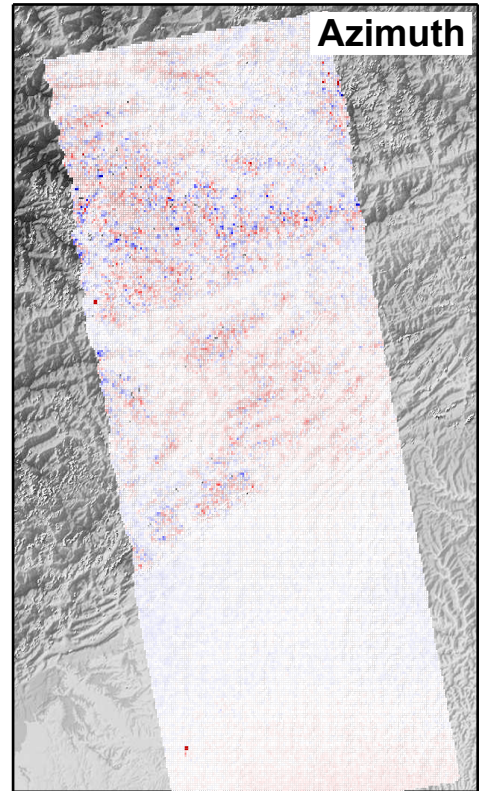
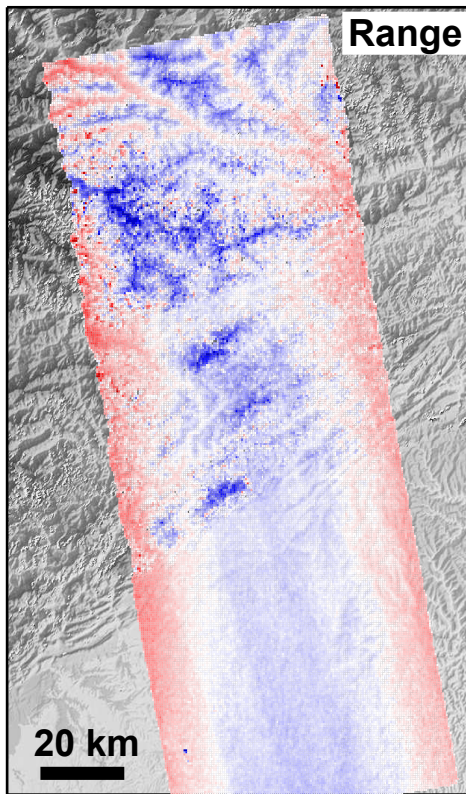


Figure S6 Preseismic offset fields calculated by conducting an elevation-dependent correction. The SAR scenes were acquired on 16 December 2007 and 31 January 2008 for the path 472 (a) and on 19 January 2008 and 5 March 2008 for the path 474 (b).

(a)

Path 472



(b)

Path 474

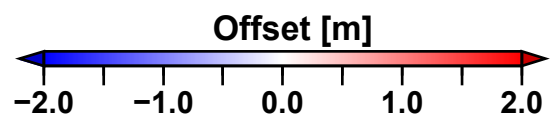
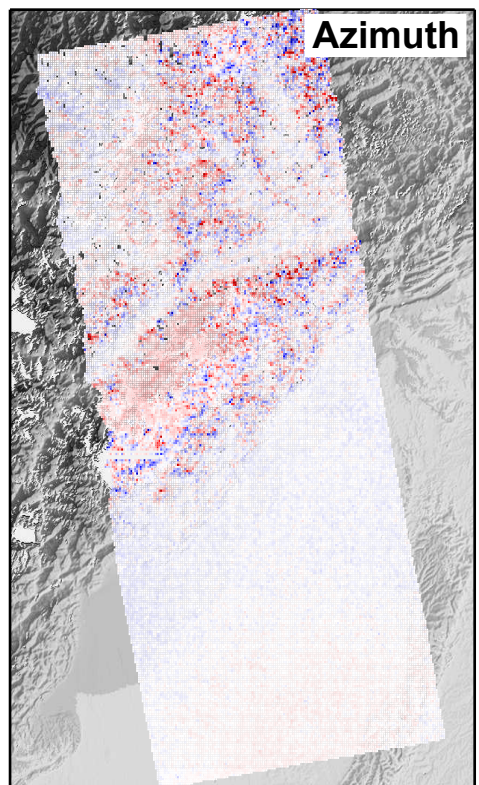
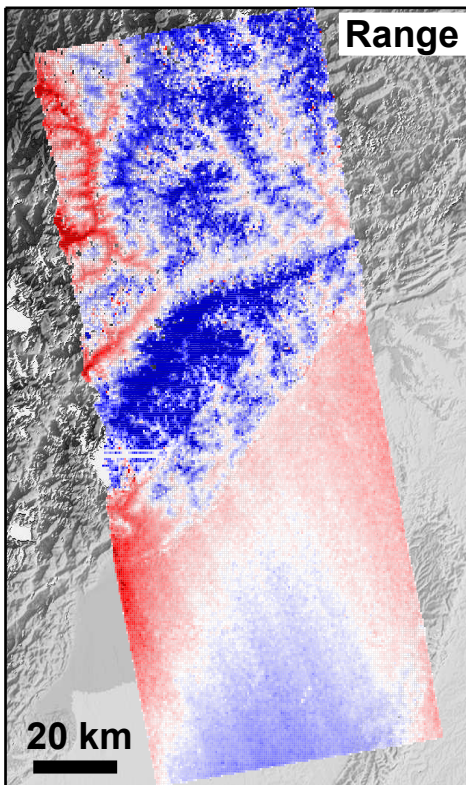


Figure S7 Same as Figure S6 but with no levation-dependent correction.